Numerical study of methanol steam reactor based on field synergy principle and analysis of different operating conditions

Shuntao Li[a], Chao Wang[a,*], Mingzheng Liao[a], Yanping Du[b,c**] Jiming Gao[d], Yanbing Wu[d]

[a] Guangdong Provincial Key Laboratory on Functional Soft Condensed Matter, School of Materials and Energy, Guangdong University of Technology, Guangzhou 510006, China

[b] School of Engineering, Lancaster University, Penryn Campus, Penryn, Cornwall TR109FE, UK

[c] China-UK Low Carbon College, Shanghai Jiao Tong University, Shanghai, 201306, China

[d] Guangdong Nengchuang Technology Co., Ltd, Guangzhou, 510000, China

Abstract

Enhanced heat and mass transfer in methanol reforming reactors to improve energy utilization is essential for efficient on-line hydrogen production. This study employed the field synergy principle to examine the impact of various pipe shapes (oval, circular, and square) on reactor performance. The results demonstrate that utilizing circular tubes enhances the overall species concentration field and velocity field, as well as the synergistic effect in the reactor, leading to enhanced methanol conversion and hydrogen production. The integration of baffles boosts the local temperature and velocity fields' synergistic effects within the reaction channel. This configuration modifies the methanol concentration gradient, decreases the synergistic angle, and enhances methanol diffusion rates, thereby facilitating its conversion. The assessment of operating parameters on reforming performance revealed that optimal conditions include a gas velocity range of 21 to 24 m/s, a weighted space velocity of 1.5 h^{-1}, a steam-to-carbon ratio of 1.1, a methanol conversion rate of 97.5%, and a CO mole fraction below 2.36 ppm.

Keywords: Methanol steam reforming; Reformer; Field synergy principle; Numerical simulation

1. Introduction

Hydrogen, recognized for its high energy density and environmental benefits, faces challenges in safe storage and transportation that hinder its widespread adoption[1-3]. On-site hydrogen production from methanol offers a promising alternative by eliminating storage risks while leveraging methanol's advantages, including stability, cost-effectiveness, and high hydrogen content under mild reforming conditions[4,5]. Methanol steam reforming is an endothermic process, which requires heat supply. Heavy trucks generate a significant amount of high-quality heat during their operation. The thermal energy contained in the exhaust gases produced can be utilized as a heat source for the methanol steam reforming reaction, thereby facilitating the recovery of waste heat.[6-9].

Methanol steam reforming (MSR) relies on compact reactors to ensure efficient heat and mass transfer. However, challenges such as uneven temperature distribution and cold spots within reaction channels impair long-term operational efficiency[10-12]. Advanced strategies to address these issues include optimizing channel geometries, employing internal and external heating configurations, and integrating flow-disturbing structures like fins or baffles to enhance heat transfer and mass diffusion. Relevant studies have shown that the installation of fins, ridges, baffle plates and other disturbed flow structures inside or outside the reaction channel can improve the heat and mass transfer performance of the reaction channel, thus significantly reducing the cold spots in the reactor[13-15]. For example, the temperature inhomogeneity on the surface of the reaction channel of a tubular fixed-bed reactor with helical fins is reduced by 48.97% compared with that of a tubular fixed-bed reactor[16]. The setup of the baffle plates grows the contact time between the reactants and the catalyst, realizing a more uniform temperature

distribution and hydrogen yield[17]. In fixed-bed reactors, the heat transfer performance outside the channel and the mass transfer performance of the reactants inside the channel can be improved by setting suitable channel geometries to increase the conversion efficiency of methanol[18]. Some researchers have designed reactor structures such as sinusoidal wave tubes, embedded channels, and diffusion pipe inlets[19-21]. Operating parameters are also one of the important factors that affect the heat and mass transfer inside the reactor. It was found that operating conditions such as reaction temperature and mass-air velocity also affect the heat and mass transfer process inside the reactor[22]. The embedded channel and the diffuser at inlet were used to improve the diffusion ability of the reactants in the reaction channel, and the uniform distribution of the reactants in the channel was favorable for the reaction. The technologies and ideas to solve the problem of uneven temperature distribution and cold spots within the reaction channel, it mainly explain the heat transfer enhancement mechanism from the flow field, while in the reactor, there is an internal heat source of the reaction, and the traditional single physical field analysis method cannot fully and accurately reflect the overall heat and mass transfer in the reactor.

Recent research highlights the importance of field synergy, wherein alignment between velocity, temperature, and concentration gradients maximizes heat and mass transfer efficiency[23,24]. This principle has been successfully applied to single physical fields but requires further exploration in multi-field systems considering chemical reactions[25,26].

This study employs numerical simulations to investigate how different pipe geometries—circular, oval, and square-impact field synergy within a methanol reactor. Operating parameters were analyzed, such as heating gas temperature and flow rate, steam-to-carbon ratio, and feed velocity. These insights aim to advance the design of

compact reactors for on-site hydrogen production with enhanced efficiency and reliability.

2. Numerical model

2.1 Reactor design

The reactor designed in this paper is to match the on-board fuel cell system (CW-HG36, China), which has an exhaust gas discharge temperature of 673 K and an exhaust volume of 246-615m^3/h during operation, and this high-temperature exhaust gas is used as the heat source of the reactor. The diffusion rate of the reactants inside the tube can be effectively increased by introducing appropriate reaction channel geometries, thus enhancing the conversion efficiency of methanol. When the gas is swept out of the reaction tube for heat transfer, the geometry affects the separation point of the gas on the tube wall and its flow direction, which in turn has an impact on the heat transfer effect between the shell side and the tube side.

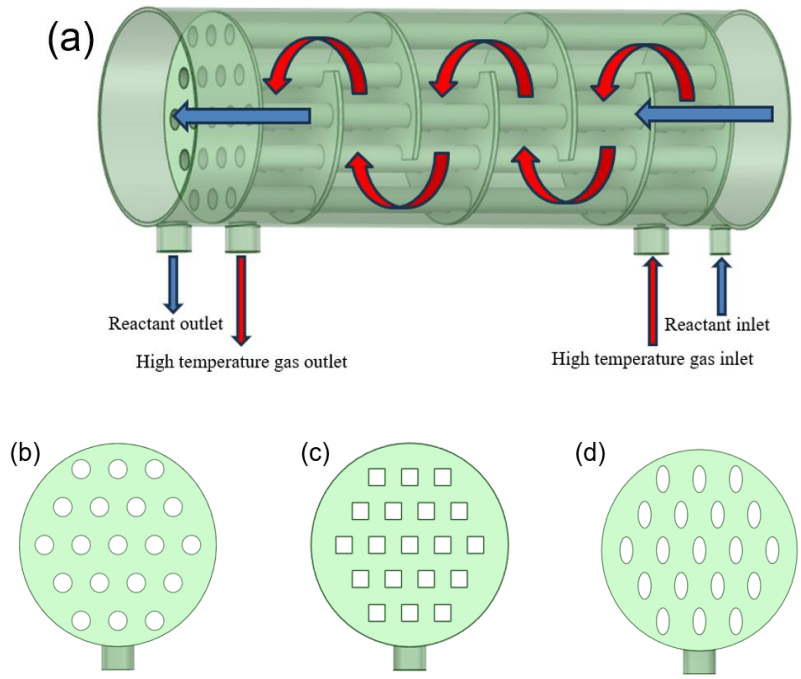

Fig. 1 (a) The structure of the methanol reformer. (b) Circular tube; (c) Square tube;（d）Oval tube.

Under the same cross-sectional area conditions, different channel structures have their own unique characteristic lengths, and thus there are differences in mass transfer

resistance[27-29]. Therefore, three basic shapes are selected for study in this paper: oval, circular, and square. The structure of the methanol reformer is shown in Fig. 1 and consists of a shell, a folding plate, and a reaction pipe. The reformer consists of two regions: the high-temperature gas flow region in the shell course (red region) and the reactant flow region in the tube course (blue region).

In the reactor, the heat consumption is divided into two parts, the energy required for the reactants to reach the reaction temperature and the energy required for the reaction. The formula for calculating the heat required is as follows:

$$Q = Q_r + Q_h \tag{1}$$

The reforming reaction is dominated by MSR, and the reaction heat of the remaining side reactions is obviously smaller than that of MSR, which will be neglected in the design calculation[30]. Q_r is the heat required for the complete conversion of methanol steam catalytic reforming; Q_h is the heat required for the reactants to reach the optimum temperature range of reforming (493K-573K).

The heat transfer area is calculated as follows:

$$S = \frac{Q}{\Delta T \hbar_s} \tag{2}$$

$$Nu = 0.71 {Re_f}^{0.5} {Pr_f}^{0.36} (Pr_f/Pr_w)^{0.25} \tag{3}$$

$$\hbar_s = \frac{Nu\lambda}{d} \tag{4}$$

Where S is the heat transfer area, and equation (3) is the zhukauskas correlation for calculating the average surface heat transfer coefficient of the fluid outwardly swept tube bundle[31]. h_s is the heat transfer coefficient of convective heat transfer, λ is the coefficient of thermal conductivity, and d is the diameter of the tube.

$$\Delta T = \frac{({T_s}^{in} - {T_t}^{in}) - ({T_s}^{out} - {T_t}^{out})}{ln\frac{({T_s}^{in} - {T_t}^{in})}{({T_s}^{out} - {T_t}^{out})}} \tag{5}$$

Where ΔT is the logarithmic mean temperature difference of the downstream heat transfer, T_s^{in} and T_s^{out} are the exhaust gas temperatures at the inlet and outlet, respectively; T_t^{in} and T_t^{out} are the reactor gas temperatures at the inlet and outlet, respectively.

Based on the heat transfer area and the size of the reaction tubes, the number of reaction tubes was determined by the following equation:

$$N_t = \frac{S}{\pi D_t L_t} \tag{6}$$

Baffles serve to support the tube bundle while maintaining the gas velocity on the shell side, increasing the flow distance and fluid turbulence. The optimal baffle cutting height is 20% to 25% of the shell diameter, and the optimal baffle spacing is 40% to 70% of the shell diameter[32]. The tube bundle is arranged in a staggered arrangement, and the fluid flows through the stretching and alternating channels between the tubes, resulting in more turbulent flow than an aligned arrangement[33]. The geometry of the reaction vessel is one of the factors affecting the heat and mass transfer performance. In this study, three pipe shapes commonly used in engineering applications were selected: circular, oval, and square. Because the geometry of the pipe affects the flow trajectory of the gas traversing its exterior, it changes the flow separation point between the gas and the pipe, resulting in different first interaction times and tailing regions between the gas and the pipe, thus affecting the heat transfer efficiency between the gas and the pipe. Under the same cross-sectional area, the pipe geometry affects the distribution of the internal gas in the axial direction, and the mass transfer rate decreases with the growth of the boundary layer. The specific structural parameters and boundary conditions are shown in Table 1.

Table 1. Reactor structural parameters and boundary conditions

Parameters	Values
Total reactor length(mm)	380
Shell bore diameter(mm)	60
Baffle distance(mm)	50
Baffle height(mm)	38
Baffle thickness(mm)	3
Reforming tube length(mm)	300
Reformer tube diameter (mm)	12
heat exchange area(m^2)	0.22
Reforming tube quantity	19
Reactor wall thickness(mm)	2
Reactant inlet temperature(K)	353
Reactant inlet velocity(m/s)	1-5
Exhaust gas inlet temperature(K)	473-623
Exhaust gas inlet velocity(m/s)	15-27

2.2 Governing equations

According to the characteristics and boundary conditions of the reforming reactor and the reforming reaction process, the following assumptions were made to simplify the analysis:

(1) All gases adopt the ideal gas incompressible model[34].

(2) The gas Reynolds number is more than 4000 in the shell side, and the

Reynolds number of the reactant in the tube phase is less than 2300, the k-ε turbulence model and laminar flow model are used in the shell side and the tube side, respectively.

(3) The diffusion process of the gas depends on the size and shape of the catalyst, the structure of the porous medium, the temperature and concentration, and the gas flow rate, in order to simplify the calculation. The catalyst bed is considered to be a porous medium with isotropic and uniform properties[35,36].

(4) The numerical calculation ignores the heat conduction and radiation of the gas[37].

(5) Ignore the effect of gravity on gas flow.

Based on the above statements and assumptions, the governing equations of CFD are as follows:

Continuity equation:

$$\frac{\partial(\rho V_i)}{\partial x_i} = 0 \tag{7}$$

Momentum equation：

$$\varepsilon\frac{\partial(\rho V_i V_j)}{\partial x_i} = -\varepsilon\frac{\partial p}{\partial x_j} + \varepsilon\frac{\partial}{\partial x_i}\left[\mu\left(\frac{\partial V_j}{\partial x_i} + \frac{\partial V_i}{\partial x_i}\right)\right] + S_m \tag{8}$$

Where ε represents the porosity, S_m represents the momentum source term generated by the porous catalyst, which can be calculated by the following equation. S_m equals to 0 in the free flow region.

$$S_m = -\frac{\mu}{k}V_i + \frac{\rho\beta}{2}V_i|V| \tag{9}$$

According to assumption (1), the mixture density of an incompressible ideal gas ρ can be calculated by equation (4):

$$\rho = -\frac{p}{RT\Sigma_i \frac{Y_i}{Mw,i}} \tag{10}$$

The dynamic viscosity μ of the gas mixture is calculated by the Wilke equation[38]:

$$\mu = \Sigma_i \frac{Y_i u_i}{\Sigma_j Y_j \varphi_{ij}} \tag{11}$$

$$\varphi_{ij} = \frac{\left[1 + \left(\frac{\mu_i}{\mu_j}\right)^{\frac{1}{2}} \left(\frac{Mw,i}{Mw,j}\right)^{\frac{1}{4}}\right]^2}{\left[8\left(1 + \frac{Mw,i}{Mw,j}\right)\right]^2} \tag{12}$$

Where Y_i is the mass fraction of species i, u_i is the dynamic viscosity of species i, and Mw,i is the relative molecular mass of species i.

The permeability κ and inertia loss coefficient β of catalyst region along each component direction are calculated by Ergun equation as follows[39]:

$$\kappa = \frac{D_p^2 \varepsilon^3}{150(1-\varepsilon)^2} \tag{13}$$

$$\beta = \frac{3.5(1-\varepsilon)}{D_p \varepsilon^3} \tag{14}$$

Energy equation：

$$\rho c_p \frac{\partial (TV_i)}{\partial x_i} = \lambda_{eff} \frac{\partial}{\partial x_i} \left(\frac{\partial T}{\partial x_i}\right) + \varepsilon S_t \tag{15}$$

The specific heat capacity c_p of the fluid is calculated by the sum of the average specific heat capacity of the mass fraction of each component. The effective thermal conductivity λ_{eff} is calculated from the thermal conductivity λ_f and λ_s of fluids and solids in a porous bed by the following equation:

$$\lambda_{eff} = \varepsilon \lambda_f + (1-\varepsilon)\lambda_s \tag{16}$$

$$\lambda_f = \Sigma_i \frac{Y_i \lambda_i}{\Sigma_j Y_j \varphi_{ij}} \tag{17}$$

Where λ_i is thermal conductivity of species i, λ_f is determined by the catalyst.

S_t is the energy source term caused by a chemical reaction and equals zero in the non-reaction domain. The calculation equation is as follows:

$$S_t = -\sum_{i=1}^{n}\left(\frac{h_i^o}{M_{w.i}} + \int_{T_{ref}}^{T} c_{p,i}\,\mathrm{d}T\right)(R_{i.r}) \tag{18}$$

Species transport equations：

$$\varepsilon\frac{\partial(c_i V_i)}{\partial x_i} = D_{eff}\frac{\partial}{\partial x_i}\left(\frac{\partial c_i}{\partial x_i}\right) + \varepsilon\sum_{r=1}^{n} M_{w.i}R_{i.r} \tag{19}$$

$$D_{eff} = D_k\varepsilon^{\tau} \tag{20}$$

2.3 Chemical kinetic modelling

This work was carried out based on a commercial CuO/ZnO/Al_2O_3 catalyst. The kinetic model of the MSR reaction has been controversial and unsolved in methanol catalytic reforming reaction systems. Therefore, several kinetic models exist to describe it, which can be classified into single-rate, dual-rate, and triple-rate models based on the number of equations involved in the MSR reaction. In the single-rate model, the SR reaction is used to represent the entire methanol reforming process, and only methanol reforming is considered; in this model, the products are only hydrogen and carbon dioxide, and the production of carbon monoxide cannot be represented. The dual-rate model usually represents the methanol reforming process with either the SR-DE or SR-rWGS reaction, but neglecting either DE or rWGS results in lower calculated than experimental values of CO concentration. The three-rate model containing the three chemical reactions SR-DE-rWGS can accurately describe the

product components in the methanol catalytic reforming reaction system, and the accuracy of the simulation results was verified experimentally. Many researchers have studied the reaction mechanism and kinetics of copper-based catalysts[40,41]. Methanol steam reforming reaction (MSR, equation 21), reverse water gas shift reaction (rWGS, equation 22) and methanol decomposition reaction (MD, equation 23) are as follows[42].

$$CH_3OH + H_2O \rightarrow CO_2 + 3H_2 \quad (21)$$

$$CO_2 + H_2 \rightarrow CO + 2H_2O \quad (22)$$

$$CH_3OH \rightarrow CO + 2H_2 \quad (23)$$

The kinetic reaction rate of the above chemical reaction is based on the Arrhenius equation and corrected by the concentration term[43]. The parameters of the catalyst and kinetic are shown in Table 2, and the reaction rates of SR, MD and rWGS are expressed by a user-defined function (UDF):

$$R_{i,SR} = k_1 C_{CH_3OH}^{0.6} C_{H_2O}^{0.4} \exp\left(\frac{E_{a1}}{RT}\right) \quad (24)$$

$$R_{i,rWGS} = k_2 C_{CO_2} C_{H_2} \exp\left(-\frac{E_{a2}}{RT}\right) - k_{-2} C_{CO} C_{H_2O} \exp\left(-\frac{E_{a2}}{RT}\right) \quad (25)$$

$$R_{i,MD} = k_3 C_{CH_3OH}^{1.3} \exp\left(\frac{E_{a3}}{RT}\right) \quad (26)$$

Where k_i is the pre-factor of the rate equation i, C_i is the molar concentration of component i, E_i is the activation energy of the chemical reaction, and the relationship between k_2 and k_{-2} is defined by the equilibrium constant of the reverse water gas shift reaction[43]:

$$k_2 * k_{-2} = K_2 \quad (27)$$

$$K_2 = exp\left(\frac{4577.8}{T} - 4.33\right) \quad (28)$$

Table 2. parameters of catalyst and kinetic model of reactions

Parameters used in this study	Values
Catalyst density(kg/m^3)	1480[44]
Catalyst layer porosity	0.38[44]
Catalyst thermal conductivity (W/m/K)	0.3[44]
Catalyst permeability(m^2)	2.379×10^{-12}[45]
Activation energy for SR (J/mol)	1.09×10^5[46]
Activation energy for rWGS (J/mol)	1.15×10^5[46]
Activation energy for MD (J/mol)	1.42×10^5[46]
Pre-exponential factor for SR	9.55×10^{12}[46]
Pre-exponential factor for rWGS	1.65×10^{13}[46]
Pre-exponential factor for MD	1.65×10^{13}[46]

2.4 Parameters definitions

Field synergy angle

The field synergy principle can be derived from the energy equation (9), according to Guo's theory[23].

$$\rho c_p \frac{\partial (TV_i)}{\partial x_i} = \lambda_{eff} \frac{\partial}{\partial x_i}\left(\frac{\partial T}{\partial x_i}\right) = -\dot{q} \tag{29}$$

After integrating equation (15) in the direction of wall thickness with dimensionless, the following equation can be obtained.

$$Nu_x = Re_x Pr \int_0^1 (\bar{U} \cdot \nabla \bar{T})\, \mathrm{d}\bar{y} \tag{30}$$

$$\beta = \cos^{-1}\left(\frac{V_i \cdot \frac{\partial T}{\partial x_i}}{|V_i|\left|\frac{\partial T}{\partial x_i}\right|}\right) \tag{31}$$

Collaborative equations based on field synergy principle of temperature, Chen et al. derived the synergy equation of mass transfer field through the field synergy principle of temperature equation[47]:

$$\alpha = cos^{-1}\left(\frac{V_i \cdot \frac{\partial c_i}{\partial x_i}}{|V_i|\left|\frac{\partial c_i}{\partial x_i}\right|}\right) \tag{32}$$

In the reactor, heat and mass transfer are included, and accompanied by changes in component concentrations, there are coupling effects between reaction and heat transfer. The synergy angle of β (Equation 31) can well characterize the heat transfer performance of the reaction region, and the better the temperature coordination, the more non-uniform the temperature distribution. The synergy angle of α (Equation 32) can reflect the distribution of species. In the chemical reaction region, the uniformity of reaction rate will be reflected in the increase of concentration synergy angle.

Weight hourly space velocity (WHSV) [48]:

$$WHSV = \frac{q_{m,in}}{m_{cat}} \tag{33}$$

Where WHSV represents weight hourly space velocity, $q_{m,in}$ and m_{cat} are the reactant inlet mass flow and catalyst mass respectively.

The following indicators are used to evaluate the performance of the reactor[34,49-52].

CH_3OH conversion：

$$X_{CH_3OH} = \frac{M_{CH_3OH,in} - M_{CH_3OH,out}}{M_{CH_3OH,in}} \times 100\% \tag{34}$$

CO selectivity：

$$S_{CO} = \frac{M_{CH_3OH,in} - M_{CH_3OH,out}}{M_{CH_3OH,in}} \times 100\% \quad (35)$$

Where X_{CH_3OH} represents the methanol conversion; $M_{CH_3OH,in}$ and $M_{CH_3OH,out}$ are the methanol mass fraction at reforming inlet and outlet, respectively.

Energy efficiency of high-temperature gas：

$$\Delta\varphi = H_{in} - H_{out} \quad (36)$$

$$\eta = \frac{Heat\ of\ Reaction}{\Delta\varphi} \times 100\% \quad (37)$$

Where $\Delta\varphi$ represents the heat release rate of the burner gas; H_{in} and H_{out} are the total sensible heat of high-temperature gas at the inlet and outlet in shell side, respectively. η represents the ratio of heat of reaction to $\Delta\varphi$.

Velocity uniformity coefficients[53]:

$$\gamma = \sqrt{\frac{\left(\sum_{i=1}^{n}\left(\frac{V_i}{\bar{V}} - 1\right)^2\right)}{N}} \quad (38)$$

Where γ represents velocity uniformity coefficients of the gas in the shell side; V_i and $\bar{V}$ are the specified average velocity of the plane and average velocity in the shell side, respectively. The smaller the γ value, the better the velocity uniformity.

2.5 Solution methods & boundary conditions

In this study, the numerical model was developed using ANSYS FLUENT 2022R1 to solve the governing equations. The SIMPLE-C algorithm was employed for pressure-velocity coupling due to its computational efficiency[54]. The laminar finite-rate kinetic model was applied to solve the species transport equations for methanol reforming reactions, while the standard k−ε model described turbulence in the shell side. Reactant flow in the catalyst bed was modeled using the porous

medium approach, assuming isotropic and homogeneous properties. Convergence was determined when the normalized residuals for all variables were less than 10^{-6}, and mass, heat flux, and outlet properties stabilized, indicating steady-state conditions. Boundary conditions included specified mass flow rate at the inlet, pressure outlet conditions, and coupled wall heat transfer between the heating and reaction channels. At the interface between free flow and the catalyst layer, continuity of temperature, velocity, concentration, and flux was ensured. The operating pressure was set to 1 atm, replicating experimental conditions and simplifying model validation.

2.6 Validation

2.6.1 Numerical model validation

To verify the accuracy and reliability of the proposed numerical model, the simulation results were compared with experimental data from Tang et al.[55]. The geometric and operating conditions of the methanol reforming unit were set to match those in Tang et al.'s study, including a methanol-to-water vapor ratio of 1:1, an inlet temperature of 373 K, and an operation pressure of 1 atm. The chemical model and other input parameters were similarly aligned. Five experiments were conducted at different air inlet temperatures to evaluate the methanol conversion rate and the molar fraction of hydrogen in the reformate gas at the outlet. As shown in Fig. 2, the simulated methanol conversion rates and hydrogen molar fractions exhibit strong agreement with the experimental results. The maximum deviation of 7.6% occurs for the hydrogen molar fraction at an air inlet temperature of 583 K, while errors under other conditions remain within 5.0%, falling within an acceptable range of experimental uncertainty. This high level of both quantitative and qualitative agreement confirms the validity of the mathematical model, demonstrating its

suitability for further investigation into the methanol steam reforming process.

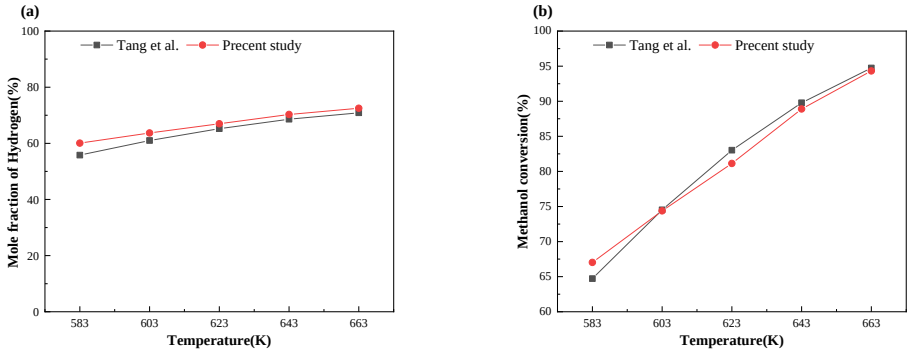

Fig. 2 Comparison with reference Tang et al. (a)mole fraction of hydrogen; (b) methanol conversion.

2.6.2 Gird independence validation

To verify the effect of grid density on the accuracy of simulation results and reduce computational cost, a grid independence test is necessary. As the performance of the methanol reforming reactor is significantly influenced by temperature, a boundary layer is introduced at the interface between the fluid and the solid regions of the reactor. This layer helps to capture the temperature and species concentration gradients near the wall, thereby enhancing the accuracy of the calculations.

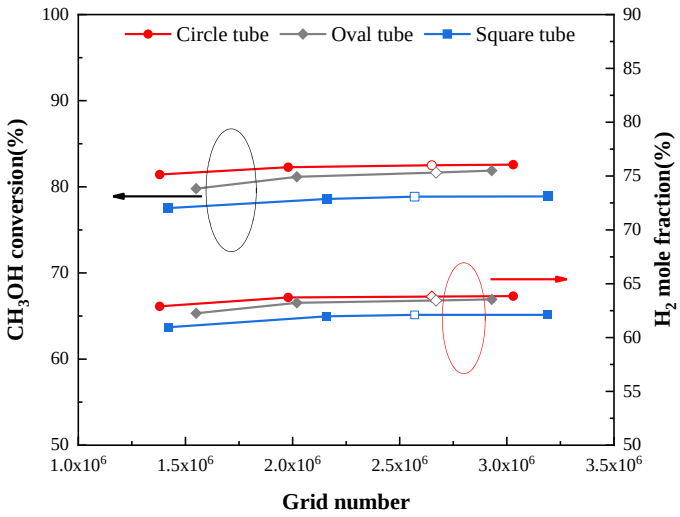

Fig. 3 Grid independence verification.

As shown in Figure 3, the number of grids affects the results of numerical calculations, mainly due to two sources: discretization error and rounding error. In this work, double-precision calculation is adopted to reduce the rounding error caused by the limited precision constraint of the computer when representing and calculating floating-point numbers; in addition, by setting grid models with different precisions to reduce the discretization error, the methanol conversion rates calculated for the circular tube, elliptical tube, and square tube under the 2.5 million grid model and the 3 million grid model only differ by 0.09%, 0.16%, and 0.02%, respectively. The continuous improvement of grid quality has little impact on the accuracy of the calculation results, and it can be considered that the influence of the number of grids on the calculation results has been eliminated. A model with 2.5 million grid numbers can be selected for subsequent simulations.

3. Results and Discussion

3.1Effect of tube geometry on heat transfer in reactor shell side

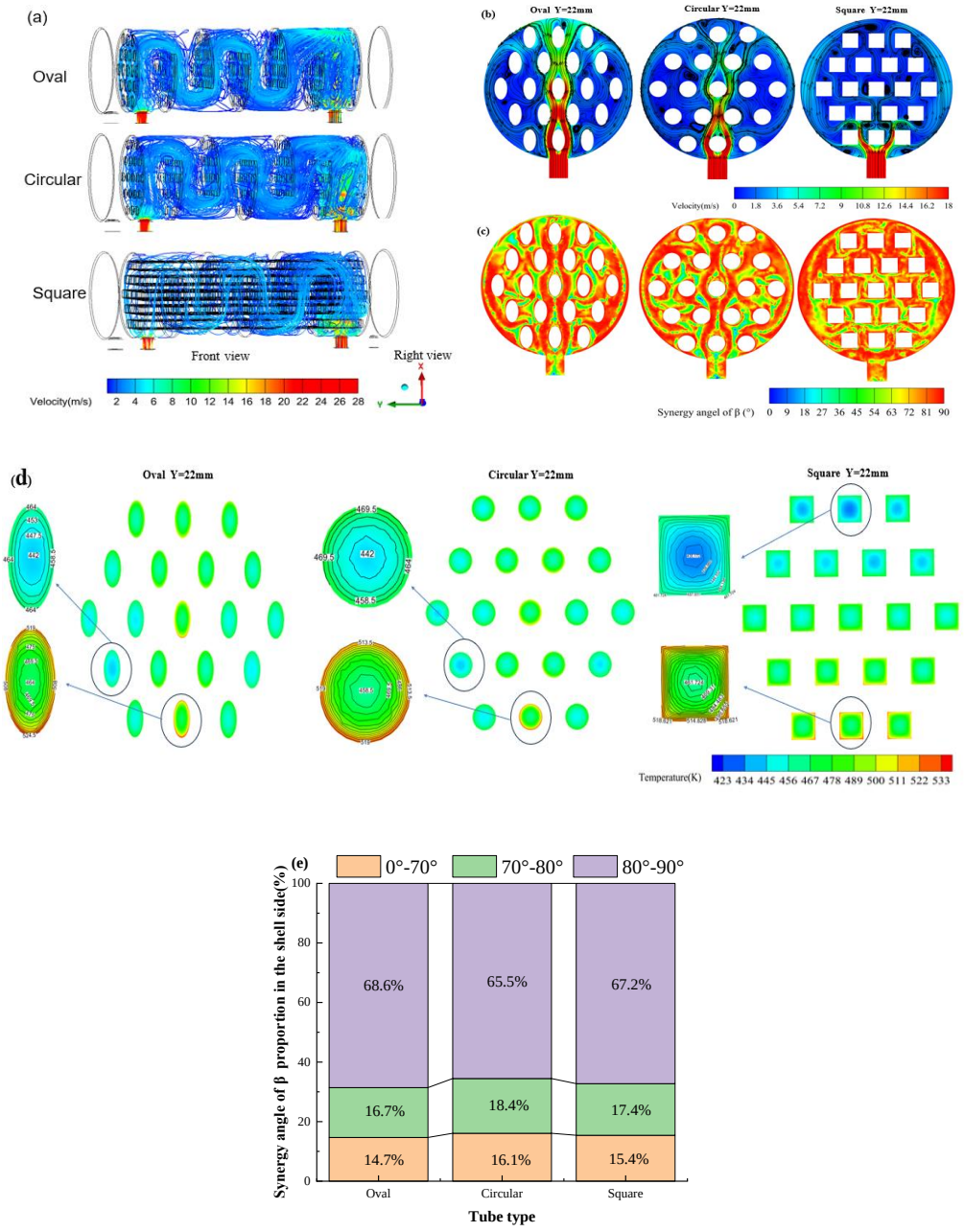

Fig. 4 (a) Velocity contour and streamline and (b) Streamline; (c) Synergy angle of β and, (d) Temperature distribution at the plane of Y=22mm (e) Synergy angle of β proportion in shell side under WHSV=2.0h^{-1}, T_{air}=573K, S/C=1.2 conditions.

Gas entering the shell side of the reactor will exhibit different flow patterns due

to the arrangement of the tubes and the geometry of the tubes. Fig 4(a) shows the effect of different tube configurations on the gas velocity and streamlines in the shell side of the reactor. It can be seen that the gas velocity distribution in the shell side is more concentrated and uniform, with a uniformity coefficient of 1.22, in the oval tube, while the uniformity coefficients are 1.09 and 0.986 in the circular and square tubes, respectively. Fig. 4(b) shows the effect of different tube configurations on the gas velocity and streamlines in the XZ-plane of the shell side of the reactor. Compared to the circular tube, the separation point of the flow in the oval tube is closer to the rear of the tube, the wake region is smaller, and the shape resistance is lower. However, the separation point of the flow in the square tube appears in a plane perpendicular to the flow direction, with a high shape resistance.

Fig. 4(c) highlights the rapid change in velocity direction within the vortex formation region, where the synergistic angle (β) is significantly lower compared to the mainstream flow region, this behavior is indicative of well coupling between the velocity and temperature gradients. Particularly in the region adjacent to the tube wall, the boundary layer, approximately 0.5 mm thick, is formed as the gas adheres to the tube wall. This region exhibits a poor heat transfer performance, with a coupling angle nearing 90°, which impedes efficient thermal exchange.

The location of the flow separation point also affects the temperature distribution within the reactor, as illustrated in Fig. 4(d). In both the oval and circular tubes, the lowest temperature occurs along the Y-axis direction. Conversely, the square tube exhibits the lowest temperature at the furthest end from the inlet. Within a single tube, the maximum temperature difference varies: 22-60K for the oval tube, 27-57K for the circular tube, and 27-57K for the square tube. The temperature peaks at the corners of the square tube, at the apex of the long axis in the oval tube, and at the region of initial

contact with the incoming flow in the circular tube, due to the symmetrical geometry of the latter.

Finally, Fig. 4(e) quantifies the volume fraction occupied by different angles in the shell course. Notably, the external region of the oval tube occupies 68.6% of the volume between 70° and 90° angles, which correlates with the lowest heat transfer efficiency in this region. In comparison, the square tube performs slightly better, while the circular tube demonstrates the highest heat transfer efficiency due to its more symmetric geometry and uniform flow characteristics.

3.2Heat and mass transfer in reactor tube side

As seen in Fig. 5(a), the temperature of both reactants and products in the reaction channel increases gradually along the flow direction. A marked temperature rise is observed in the 15mm section of the reaction channel after the baffle. This sudden temperature change introduces a notable coupling between the temperature and velocity fields within the reaction channel.

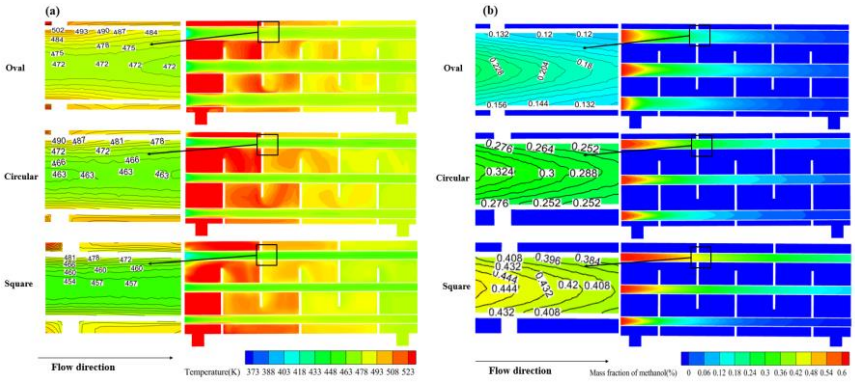

Fig. 5 Effect of tube structure (a) Temperature distribution and (b) Mass fraction of methanol distribution at the plane of Z=0mm under WHSV=2.0h^{-1}, T_{air}=573K, S/C=1.2 conditions.

For instance, in the case of the circular tube, as shown in Fig. 6(a), the synergy angle of β (the angle between the temperature and velocity gradient) increases slightly

at the baffle positions (Y = 50, 100, 150, 200, 250mm). After this point, the angle decreases within the subsequent 5mm (Y = 100–105mm, Y = 150–155mm, Y = 200–205mm, Y = 250–255mm) to a minimum of approximately 86.0°, before returning to a value similar to the pre-baffle region after another 10mm.

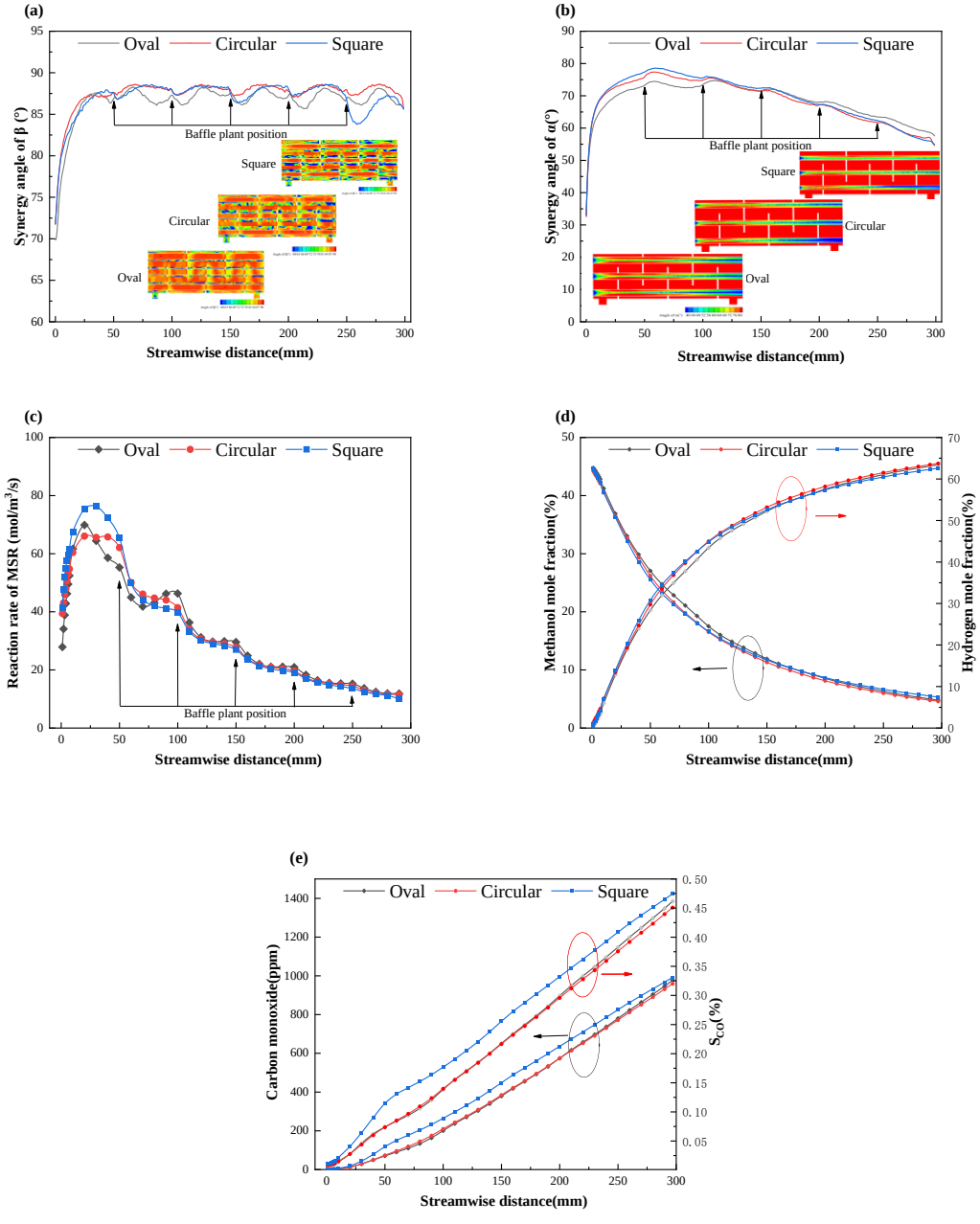

Fig. 6 (a) Synergy angle of β; (b) Synergy angle of α; (c)Reaction rate of MSR; (d) Methanol and hydrogen mole fraction; (e) Carbon monoxide mole fraction and S_{CO} alone the tube side under WHSV=2.0h^{-1}, Tair=573K, S/C=1.2 conditions.

This observed change in β is attributed to the effect of the baffle on radial heat transfer, as shown in Fig. 6(b), which lowers synergistic angle of β and strengthens the heat transfer in the local region. For example, at Y = 50 mm in the circular tube, the temperature gradient direction points towards the wall, creating a perpendicular relationship with the velocity gradient, thus increasing the synergistic angle. However, downstream of the baffle, the temperature gradient shifts towards the flow direction, reducing the angle and demonstrating the delayed effect of the baffle on the temperature-velocity coupling.

In Figure 6 (a), it can be seen that the synergy angle and the methanol reaction rate change periodically, and the methanol reaction rate is mainly affected by temperature, so it can be represented by temperature change. The expression of synergy angle change and the expression of temperature change are, respectively:

$$Y_\beta = 88.1 + 0.52 \sin\left(\frac{\pi(x-8.5)L}{2}\right) \tag{39}$$

$$Y_t = 469.6 + 0.74 \sin\left(\frac{\pi(x-32)L}{2}\right) \tag{40}$$

Where L is the baffle spacing. Therefore, the delay distance of the synergy angle can be calculated as follows:

$$F = \frac{\pi(x-8.5)L}{2} - \frac{\pi(x-32)L}{2} \tag{41}$$

Furthermore, Fig. 6(b) indicates that the methanol reaction rate is elevated at the baffle position due to increased heat transfer, whereas Fig. 6(c) confirms that the methanol distribution remains consistent with previously published studies[56]. Fig. 5(b) suggests that while the temperature gradient changes, the overall distribution pattern of methanol does not change; instead, the concentration gradient direction is altered, leading to a temporary increase in the synergistic angle of α. This effect

persists for approximately 10 mm downstream of the baffle. As observed in Fig. 6(d), both methanol and hydrogen concentrations decrease along the flow direction. This correlates with the results in Fig. 6(b), where the reduced concentration of reactants leads to a diminishing reaction rate. Fig. 6(e) shows the variation in the molar fraction of carbon monoxide along the flow direction. In the circular tube, the carbon monoxide mole fraction is the lowest, at only 959.2 ppm, which is 1.8% and 3.9% lower than in the oval and square tubes, respectively. This trend follows the order: circular < oval < square, indicating that shape and flow geometry influence the formation of by-products like CO. The increase in temperature enhances side reactions, such as methanol decomposition (MD) and reverse water-gas shift (rWGS), which have higher activation energies compared to the main reforming reaction (MSR), leading to an increase in CO selectivity.

3.3 Effects of operational parameters on the reforming performance

3.3.1 Effects of the Inlet Velocity

To investigate the impact of gas flow rate on heat transfer and methanol reforming reactions, numerical simulations were conducted for combustion gas flow rates ranging from 15 to 27 m/s. As shown in Figs. 7(a) and (b), the methanol conversion rate and carbon monoxide content both increase as the inlet velocity increases, while the square channel has the worst performance (all data in Section 3.3 are based on the average face value of the reactor outlet). And the average synergy angle of α (a measure of the interaction between the velocity and methanol mass fraction gradients) in the circular tube ranges from 62.23° to 67.62°. This is consistently 2.98%–3.77% smaller than the synergy angle of α in the oval tube and 4.26%–4.79% smaller than that in the square tube, indicating that methanol has a stronger diffusion ability in the circular tube. With increasing gas velocity, methanol

absorbs more heat, leading to an increase in the reaction rate. The increase of heat transfer decreases the radial temperature gradient, and the reaction rate tends to be uniform, resulting in a decrease in the mass fraction gradient of methanol. As a result, the methanol synergy angle increases across all tube geometries: from 64.6° to 69.6° in the oval tube, 62.2° to 67.6° in the circular tube, and 65.3° to 70.9° in the square tube. Notably, the square tube experiences the largest increase, indicating that higher gas velocity is more detrimental for methanol conversion in the square tube due to its larger surface area and longer residence time, thus showing a more homogeneous methanol distribution.

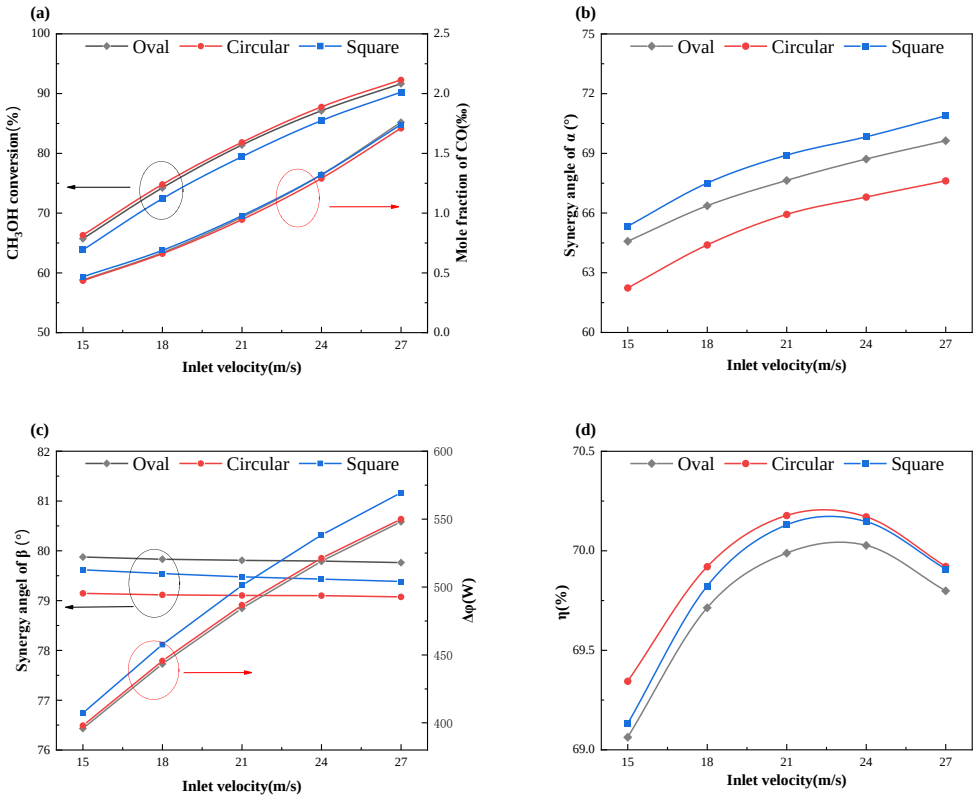

Fig. 7 Simulation results of (a) Methanol conversion; (b)Synergy angle of *α*; (c) Synergy angle of β and Δφ; (d) η under different inlet velocity

As shown in Fig. 7(c), increasing the gas velocity does not significantly improve the overall temperature field synergy, in line with findings by Liu et al.[47]. However,

under the influence of different tube geometries and internal chemical reactions, the circular tube exhibits superior temperature field coordination, with a synergy angle of 79.1°. This is due to the fact that the square tube, which has the highest flow resistance, results in the longest residence time for gas in the shell side, followed by the circular and oval tubes. Consequently, the square tube absorbs the most heat, with an average heat absorption rate of 494.7W, compared to 480.2W in the circular tube and 478.1W in the oval tube.

The high-temperature gas not only supplies heat for the reforming reaction but also raises the temperature of the reactants and products. Fig. 7(d) shows the ratio of heat used for the reaction to the total system heat. The ratio increases from 69.1% to 70.0% between 21 and 24 m/s before slightly declining. This peak indicates that, prior to reaching this point, most of the heat absorbed by the catalyst bed is used for the reforming reaction. After this peak, the excess heat raises the temperature of the reactants and products, which can promote side reactions, such as methanol decomposition (MD) and the reverse water-gas shift (rWGS) reaction. These side reactions are endothermic and have higher activation energies than the methanol reforming reaction, resulting in increased CO formation. This is undesirable in hydrogen production, as higher CO levels can lower the purity of the produced hydrogen.

3.3.2 Effects of the WHSV

To analyze the impact of Weight Hourly Space Velocity (WHSV) on the reactor's heat and mass transfer performance, simulations were carried out for WHSV values ranging from 1.0 h^{-1} to 3.0 h^{-1}. As shown in Fig. 8(a), when WHSV increases from 1.0 h^{-1} to 1.5 h^{-1}, methanol conversion rates decrease across all tube geometries: from 99.9% to 96.8% in the oval tube, 97.6% to 95.3% in the circular tube, and 95.3%

to 92.4% in the square tube, representing a reduction of approximately 3%. This decrease is primarily due to shorter contact times between the methanol and the catalyst, which lowers conversion efficiency. However, when WHSV exceeds 1.5h^{-1}, the conversion rate drops more significantly, from 96.8%, 97.6%, and 95.3% to 55.8%, 56.2%, and 55.6% in the oval, circular, and square tubes, respectively. Meanwhile, the molar fraction of carbon monoxide falls sharply by around 90% at lower WHSV, with values reducing from 13.1‰ to 2.4‰ (oval), 13.3‰ to 2.7‰ (circular), and 14.5‰ to 3.7‰ (square).

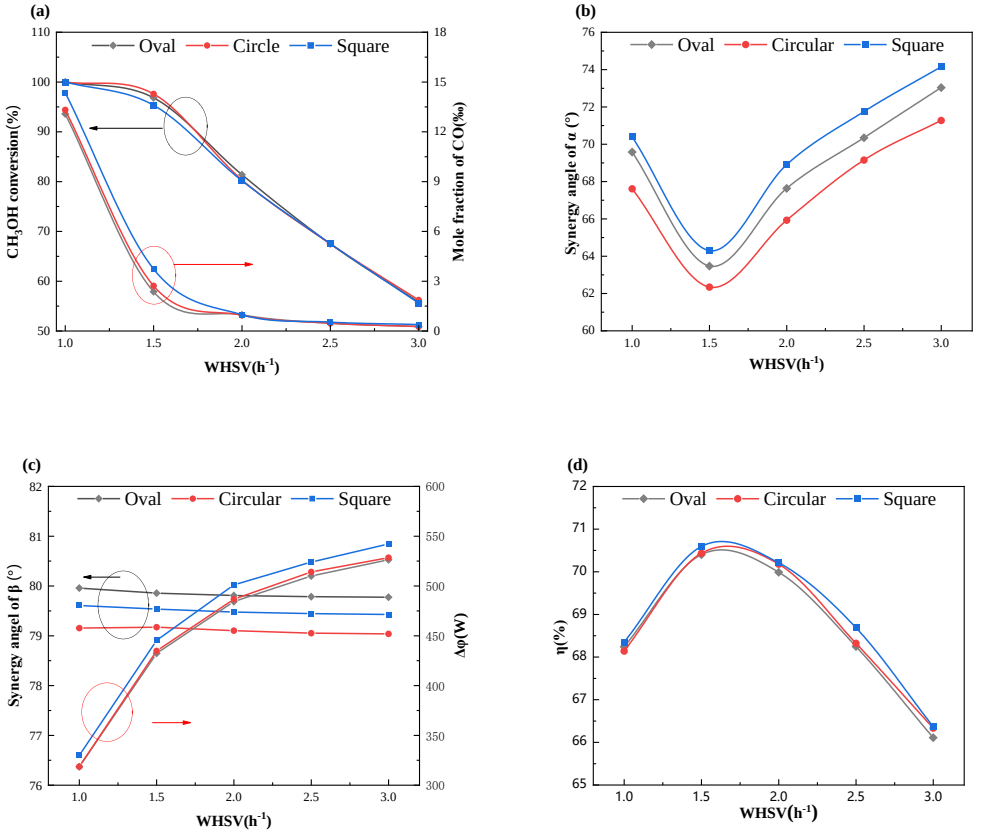

Fig. 8 Simulation results of (a) Methanol conversion; (b)Synergy angle of α; (c) Synergy angle of β and Δφ; (d) η under different WHSV

The reduced methanol conversion at higher WHSV can be attributed to the decreased contact time for reactants with the catalyst, as well as the resulting heat transfer limitations. As WHSV increases beyond 2.0h^{-1}, the flow velocity rises, and

the velocity boundary layer effect becomes more pronounced. This leads to a situation where the reactants in the center of the tube have less time to interact with the catalyst, while heat transfer from the tube wall to the center is delayed. Consequently, methanol is less uniformly distributed, with a higher concentration near the core of the flow. This is reflected in the increased methanol molar fraction gradient in the radial direction (Fig. 8(b)). The synergy angle of α, which indicates the efficiency of methanol diffusion, is smallest (62.3°) in the circular tube at WHSV = 1.5h^{-1}, suggesting optimal mass transfer conditions. At this WHSV, methanol distribution is more nonuniform, enhancing mixing and reaction rates. In general, the diffusion capacity of methanol follows the order: circular > oval > square tubes.

Fig. 8(c) shows that the synergy angle of β, which is more influenced by tube geometry than by operational parameters, also decreases with increasing WHSV. As WHSV increases, the quantity of heat absorption increases, especially noticeable between 2.5h^{-1} and 3.0h^{-1} in the oval tube, where the heat absorption rate drops significantly. This is because the higher gas velocity associated with increased WHSV reduces the contact time available for reactants and catalysts, but provides a larger temperature difference between the tube side and shell side, which improves overall heat absorption.

Fig. 8(d) reveals the effect of WHSV on the heat utilization efficiency (η). η initially increases as WHSV rises, peaking between 1.5 and 2.0h^{-1}, with peak values of 70.4% in the oval and circular tubes, and 70.6% in the square tube. This suggests that the catalyst in the reformer reaches its maximum processing capacity at WHSV values between 1.5 and 2.0h^{-1}. After this peak, further increases in WHSV lead to diminishing returns in heat absorption efficiency, as more heat is used to elevate the temperature of reactants and products rather than driving the primary chemical

reactions.

3.3.3 Effects of the S/C

The molar ratio of steam to carbon (S/C) plays a critical role in the efficiency of hydrogen production, particularly influencing methanol conversion and carbon monoxide content. As shown in Fig. 9(a), an increase in the steam content leads to a decrease in carbon monoxide (CO) concentration, which is negatively correlated with the S/C ratio. This occurs because the higher steam content promotes the reverse water gas shift (rWGS) reaction, which consumes CO, thus reducing its level in the product stream. Specifically, at an S/C of 1.5, the methanol conversion rates in oval, round, and square tubes are 87.0%, 87.7%, and 85.0%, respectively, with the circular tube exhibiting the highest conversion rate. This is due to the more nonuniform distribution of methanol vapor inside the circular tube, which enhances the interaction with the catalyst.

As the S/C ratio increases, the relative content of water vapor rises while the methanol vapor content decreases, as shown in Fig. 9(b). The increased steam promotes the methanol reforming reaction (MSR) and inhibits methanol decomposition, leading to higher conversion efficiency. This also results in a decrease in methanol vapor in the reactor, particularly in the circular tube, where the distribution of methanol is more uniform at S/C of 1.2.

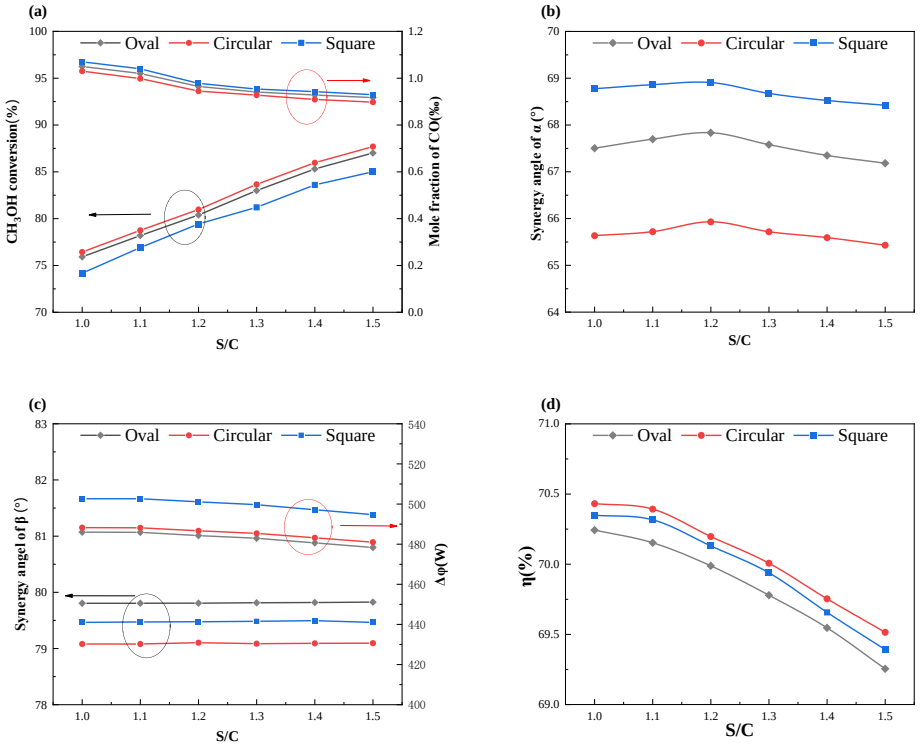

Fig. 9 Simulation results of (a) Methanol conversion; (b) Synergy angle of α; (c) Synergy angle of β and Δφ; (d) η under different S/C.

Fig. 9(c) shows the temperature synergy and heat absorption trends with varying S/C, which follow a similar pattern to those observed with different WHSV values. The endothermic nature of the chemical reactions is the primary driver for heat transfer. As shown in Fig. 9(d), with the S/C ratio increases, the total methanol content decreases, reducing the energy required for the reaction. Consequently, the total heat absorption also decreases. This is because the higher steam content, which has a higher specific heat than methanol, absorbs more heat to raise the temperature of the reactants, rather than directly contributing to the reaction itself. The decrease in methanol vapor fraction and the corresponding increase in water vapor lead to a greater proportion of heat being used to heat the reactants to the necessary reaction temperature, rather than driving the reforming reactions. This reduces the overall efficiency of heat utilization, as less heat is available for the reactions themselves.

Thus, the increase in S/C improves methanol conversion by promoting the methanol reforming reaction and suppressing side reactions. However, it also leads to reduced heat absorption efficiency due to the higher specific heat of water vapor, which is less effective in driving the reforming reactions compared to methanol vapor.

4. Conclusion

This study provides heat and mass transfer dynamics for different pipe geometries (oval, circular, and square) in a methanol reformer. The application of synergy theory enables a deeper understanding of the interrelationship between temperature and species gradients within the reactor, revealing how these interactions influence both methanol conversion and side reaction formation. Specifically, the results demonstrate how the gas flow separation points—determined by tube geometry—affect boundary layer formation and heat transfer, with the circular tube offering the most favorable temperature distribution and efficiency. Furthermore, the synergy analysis highlights the critical role of baffle plates, which cause temperature gradient discontinuities that alter the methanol concentration gradient and synergistic angles. In terms of operational parameters, the optimal conditions for methanol reforming were identified at a gas velocity of 21-24m/s, WHSV of 1.5h^{-1}, and an S/C ratio of 1.1. Under these conditions, methanol conversion reached 97.5%, with CO mole fraction kept below 2.36‰. These findings provide critical insights for enhancing reactor efficiency, guiding the design of reformers for maximum hydrogen production, and minimizing side reactions and offer both scientific and engineering contributions to the field of methanol reforming.

In this paper, the heat and mass transfer process of endothermic reaction and the field synergy principle of methanol reforming for hydrogen production in the reactor are discussed. However, the effect of exothermic reaction on the field synergy in the reactor is not discussed. Therefore, in future studies, it is necessary to further explore the influence of exothermic reaction on heat and mass transfer in the reactor and optimize the reactor involved.

Conflicts of interest

There are no conflicts to declare.

Acknowledgments

This work was supported by the National Key Research and Development Program of Intergovernmental International Cooperation Projects (No. 2022YFE0198800) and supported by the Natural Science Foundation of China (NO. 22378073)

References:

[1] Lebrouhi BE, Djoupo JJ, Lamrani B, Benabdelaziz K, Kousksou T. Global hydrogen development - A technological and geopolitical overview. INT J HYDROGEN ENERG. 2022; 47:7016-48.

[2] Le PA, Trung VD, Nguyen PL, Bac PT, Natsuki J, Natsuki T. The current status of hydrogen energy: an overview. RSC ADV. 2023; 13:28262-87.

[3] Moradi R, Groth KM. Hydrogen storage and delivery: Review of the state of the art technologies and risk and reliability analysis. INT J HYDROGEN ENERG. 2019; 44:12254-69.

[4] Tang Y, Long W, Wang Y, Xiao G, Wang Y, Lu M. Multi-objective optimization of methanol reforming reactor performance based on response surface methodology and multi-objective particle swarm optimization coupling algorithm for on-line hydrogen production. ENERG CONVERS MANAGE. 2024; 307:118377.

[5] Fan S, Chen Y, Wang Y, Huang H, Bai K, Wen H, et al. A flow-through catalytic membrane micro-reactor for hydrogen production by methanol steam reforming. CHEM ENG SCI. 2023; 282:119283.

[6] Liu H, Li Y, Lu C, Zhang Z, Xiang G, Yang X, et al. Design and operation

performance of the plate-heat transfer type hydrogen production reactor for bio-methanol reforming. BIORESOURCE TECHNOL. 2023; 386:129509.

[7]Hu S, Cui X, Yang L. Thermal matching characteristics in an autothermal methanol reforming microchannel reactor for hydrogen production. CHEM ENG SCI. 2023; 280:118987.

[8] Zhao N, Wang J, Yao Z, Shao Y, Tian Y, Liu W. A novel multi-objective optimization model of solar-driven methanol steam reforming system combining response surface methodology and three-dimensional numerical simulation. ENERG CONVERS MANAGE. 2024; 300:117986.

[9]Pashchenko D. Thermochemical waste-heat recuperation as on-board hydrogen production technology. INT J HYDROGEN ENERG. 2021; 46:28961-8.

[10]Wang F, Wang G. Performance and cold spot effect of methanol steam reforming for hydrogen production in micro-reactor. INT J HYDROGEN ENERG. 2016; 41:16835-41.

[11]Mao X, Li W, Yuan Y, Yang L. Numerical analysis of methanol steam reforming reactor heated by catalytic combustion for hydrogen production. INT J HYDROGEN ENERG. 2022; 47:14469-82.

[12]Achomo MA, Kumar A, Peela NR, Muthukumar P. Hydrogen production from steam reforming of methanol: A comprehensive review on thermodynamics, catalysts, reactors, and kinetic studies. INT J HYDROGEN ENERG. 2024; 58:1640-72.

[13]Ha C, Zhou Z, Qin J, Wang C, Liu Z, Leng S. Structural optimization calculation of methanol spiral tube reformer based on waste heat utilization and experimental verification of reactor performance. RENEW ENERG. 2024; 226:120313.

[14]Chein R, Chen Y, Chung JN. Numerical study of methanol–steam reforming and methanol–air catalytic combustion in annulus reactors for hydrogen production. APPL

ENERG. 2013; 102:1022-34.
[15]Chu X, Zeng X, Zheng T, Zhuang W, Yang Y, Zhou W, et al. Structural design and performance research of methanol steam reforming microchannel for hydrogen production based on mixing effect. INT J HYDROGEN ENERG. 2020; 45:20859-74.
[16]Zhang H, Xu C, Yu H, Wu H, Jin F, Xiao F, et al. Enhancement of methanol steam reforming in a tubular fixed-bed reactor with simultaneous heating inside and outside. ENERGY. 2022; 254:124330.
[17]Xie R, Sun J, Shi Y, Wei J. Baffled-type thermochemical reactor for high-efficient hydrogen production by methanol steam reforming. INT J HYDROGEN ENERG. 2023; 48:23425-39.
[18]Lu W, Zhang R, Toan S, Xu R, Zhou F, Sun Z, et al. Microchannel structure design for hydrogen supply from methanol steam reforming. CHEM ENG J. 2022; 429:132286.
[19]Wang D, Zhou P, Tang J, Yang L, Jie D. Numerical simulation of catalytic reaction kinetics in a sine wave tubular methanol steam reforming reactor. INT J HYDROGEN ENERG. 2024; 60:82-93.
[20]Liu S, Du P, Jia H, Zhang Q, Hao L. Study on the impact of methanol steam reforming reactor channel structure on hydrogen production performance. RENEW ENERG. 2024; 228:120612.
[21]Perng S, Horng R, Wu H. Effect of a diffuser on performance enhancement of a cylindrical methanol steam reformer by computational fluid dynamic analysis. APPL ENERG. 2017; 206:312-28.
[22]Pashchenko D. Low-grade heat utilization in the methanol-fired gas turbines through a thermochemical fuel transformation. THERM SCI ENG PROG. 2022; 36:101537.

[23] Guo ZY, Li DY, Wang BX. A novel concept for convective heat transfer enhancement. INT J HEAT MASS TRAN. 1998; 41:2221-5.
[24] Chen Q, Ren J, Guo Z. Field synergy analysis and optimization of decontamination ventilation designs. INT J HEAT MASS TRAN. 2008; 51:873-81.
[25] Che X, Wu F, Wang J. Experiment, CFD simulation and field synergy characteristics analysis of hot-air drying process in a spouted bed. POWDER TECHNOL. 2024; 438:119687.
[26] Zhang X, Zhang X, Bao C, Lai N. Numerical study and field synergy analysis on CO selective methanation packed-bed reactor. INT J HYDROGEN ENERG. 2023; 48:25144-57.
[27] Chen J, Li T. Design Issues of Thermally Integrated Methanol Reforming Systems for the Production of Hydrogen: Effects of Channel Dimensions and Catalyst Properties. ENERG FUEL. 2019; 33:12026-40.
[28] Tran N, Wang C. Effects of tube shapes on the performance of recuperative and regenerative heat exchangers. ENERGY. 2019; 169:1-17.
[29] Dogan S, Darici S, Ozgoren M. Numerical comparison of thermal and hydraulic performances for heat exchangers having circular and elliptic cross-section. INT J HEAT MASS TRAN. 2019; 145:118731.
[30] Khan MMN, Jayanti S. Minimizing Heat Transfer Resistance in an Integrated Methanol Steam Reformer Designed Using Space-Filling Curves. IND ENG CHEM RES. 2022; 61:5255-71.
[31] Zhukauskas AA. Convective heat transfer in external flows. Journal of engineering physics. 1987.
[32] Ambekar AS, Sivakumar R, Anantharaman N, Vivekenandan M. CFD simulation study of shell and tube heat exchangers with different baffle segment configurations.

APPL THERM ENG. 2016; 108:999-1007.

[33]Wang J, Sun Z, Liu X. Heat transfer and flow characteristics in a rectangular channel with miniature square column in aligned and staggered arrangements. INT J THERM SCI. 2020; 155:106413.

[34]Hu Y, Han C, Li W, Hu Q, Wu H, Li Q. Investigation of methanol steam reforming reformer heated by catalyst combustion for kW-scale fuel cell. THERM SCI ENG PROG. 2023; 45:102114.

[35]Pashchenko D. Intra-particle diffusion limitation for steam methane reforming over a Ni-based catalyst. FUEL. 2023; 353:129205.

[36]Karpilov I, Papkov V, Pashchenko D. Comparative analysis of diffusion mechanisms inside porous media for steam methane reforming over Ni-Al 2O 3 catalyst. INT COMMUN HEAT MASS. 2024; 159:108322.

[37]Perng S, Chien T, Horng R, Wu H. Performance enhancement of a plate methanol steam reformer by ribs installed in the reformer channel. ENERGY. 2019; 167:588-601.

[38]Wilke CR. A Viscosity Equation for Gas Mixtures. The Journal of Chemical Physics. 1950; 18:517-9.

[39]Ergun S, Orning AA. Fluid Flow through Randomly Packed Columns and Fluidized Beds. Industrial and engineering chemistry. 1949; 41:1179-84.

[40]Wu D, Jiang Y, Zhang C, Han J, Wang H, Liu Y, et al. Synergistic metal-support interaction promoting the formation of oxygen vacancies and their role in CO-PROX over CuO/NiO-CeO2 catalyst. Journal of Environmental Chemical Engineering. 2024; 12:111818.

[41]Qiao W, Zhang L, Zhang K, Zheng Y, Zhang C, Han J, et al. Low temperature synthesis of Cu1−xAl2.5 spinel solid solution as sustained release catalyst for

methanol to hydrogen. INT J HYDROGEN ENERG. 2022; 47:32133-44.
[42] PEPPLEY BA, AMPHLETT JC, KEARNS LM, MANN RF. Methanol-steam reforming on Cu/ZnO/Al2O3 catalysts. Part 2. A comprehensive kinetic model. Applied catalysis. A, General. 1999; 179:31-49.
[43] Purnama H, Ressler T, Jentoft RE, Soerijanto H, Schlögl R, Schomäcker R. CO formation/selectivity for steam reforming of methanol with a commercial CuO/ZnO/Al2O3 catalyst. Applied Catalysis A: General. 2004; 259:83-94.
[44] Yao L, Wang F, Wang L, Wang G. Transport enhancement study on small-scale methanol steam reforming reactor with waste heat recovery for hydrogen production. ENERGY. 2019; 175:986-97.
[45] Bose D, Kumar I, Hens A. Performance analysis of methanol steam micro-reformers for enhanced hydrogen production using CFD. Chemical Engineering Research and Design. 2023; 196:297-308.
[46] Hsueh C, Chu H, Yan W, Leu G, Tsai J. Three-dimensional analysis of a plate methanol steam micro-reformer and a methanol catalytic combustor with different flow channel designs. INT J HYDROGEN ENERG. 2011; 36:13575-86.
[47] Liu W, Liu P, Dong ZM, Yang K, Liu ZC. A study on the multi-field synergy principle of convective heat and mass transfer enhancement. INT J HEAT MASS TRAN. 2019; 134:722-34.
[48] Gribovskiy AG, Makarshin LL, Andreev DV, Klenov OP, Parmon VN. Thermally autonomous microchannel reactor to produce hydrogen in steam reforming of methanol. CHEM ENG J. 2015; 273:130-7.
[49] Chein R, Chen Y, Zhu H, Chung JN. Numerical Simulation of Flow Disturbance and Heat Transfer Effects on the Methanol-Steam Reforming in Miniature Annulus Type Reformers. ENERG FUEL. 2012; 26:1202-13.

[50] Klenov OP, Makarshin LL, Gribovskiy AG, Andreev DV, Parmon VN. CFD modeling of compact methanol reformer. CHEM ENG J. 2015; 282:91-100.

[51] Ghasemzadeh K, Harasi JN, Amiri TY, Basile A, Iulianelli A. Methanol steam reforming for hydrogen generation: A comparative modeling study between silica and Pd-based membrane reactors by CFD method. FUEL PROCESS TECHNOL. 2020; 199:106273.

[52] Qiao W, Yang S, Zhang L, Tian Y, Wang H, Zhang C, et al. Performance ofCu-Ce /M-Al (M = Mg, Ni, Co, Zn) hydrotalcite derived catalysts for hydrogen production from methanol steam reforming. INT J ENERG RES. 2021; 45:12773-83.

[53] Li C, Huang P, Pan M. Reverse optimization algorithm of velocity uniformity in microchannels based on a simplified resistance network model. CHEM ENG SCI. 2020; 221:115655.

[54] Mirvakili A, Bakhtyari A, Rahimpour MR. A CFD modeling to investigate the impact of flow mal-distribution on the performance of industrial methanol synthesis reactor. APPL THERM ENG. 2018; 128:64-78.

[55] Tang Y, Wang Y, Long W, Xiao G, Wang Y, Li W. Analysis and enhancement of methanol reformer performance for online reforming based on waste heat recovery of methanol-diesel dual direct injection engine. ENERGY. 2023; 283:129098.

[56] Kusumastuti R, Sasmoko, Cheng P, Tseng C. A numerical study of internally heating, counter-flow tubular packed bed reactor for methanol steam reforming. INT J HYDROGEN ENERG. 2024; 52:964-77.